Numerical optimization of evaporative cooling in artificial gas diffusion layers

Sarah van Rooij[a], Mirco Magnini[b], Omar K. Matar[c], Sophia Haussener[a,*]

[a]*Institute of Mechanical Engineering, École Polytechnique Fédérale de Lausanne, Switzerland*
[b]*Department of Mechanical, Materials and Manufacturing Engineering, University of Nottingham, U.K.*
[c]*Department of Chemical Engineering, Imperial College London, London, U.K.*

Abstract

The utilization of evaporative cooling in the gas diffusion layers (GDLs)of fuel cells or electrolyzers can effectively dissipate the heat produced by high power density operation, thus leading to economically more competitive electrochemical cells. The highly porous GDLs offer a large surface area, allowing to cope with larger heat fluxes and leading to larger evaporation rates. The understanding of the best GDL structure and cell operating conditions for optimized cooling is difficult to determine, given the complexity of the multi-physical processes involved. A direct pore-level numerical modeling framework was developed to analyze the heat and mass transport phenomena occurring within GDLs with integrated evaporative cooling. A three-dimensional model was developed that solves the Navier-Stokes equations, species transport and energy conservation equations in the gas domain, and energy conservation equations in the stagnant fluid phase and solid phase. Evaporation at the liquid-vapor interface was modeled using kinetic theory. The GDL geometry was approximated by an artificial lattice so as to enable the analysis of the effect of a systematic change in the geometry on the transport and evaporation characteristics. A parametric study indicated that increasing the GDL's porosity from 0.8 to 0.9 and the operating temperature from 60 °C to 80 °C led to an increase of the evaporation rate of 19.9% and 197%, respectively. Changing the thermophysical properties of the carrier gas (air to hydrogen) enhanced the evaporation rate, and therefore the cooling of the GDL, by a factor 2.7. The decrease of the amount of vapor in the carrier gas at the water-gas interface impacted positively the evaporative cooling in the GDL.

Keywords: Gas diffusion layers, Artificial lattice, Pore-scale modeling, Evaporative cooling, Kinetic gas theory

1. Introduction

Fuel cells and electrolyzers will be an important asset in a future, more sustainable energy economy. Proton exchange membrane (PEM) electrochemical cells are particularly interesting as they seem to better deal with dynamic load profiles [1], [2]. For economical reasons, they are designed for high power density operation, which results in larger heat generated and, correspondingly, increased temperature of the PEM cell. Cooling techniques are required to efficiently dissipate waste heat and to ensure operation at optimal temperature. Conventional PEM electrochemical cells utilize heat exchangers for cooling and water recirculation loops for reactant gas humidification. These complex and costly auxiliary components [3], [4] can be replaced altogether by implementing evaporative cooling in gas diffusion layers (GDLs), which may simultaneously provide the functionality of efficient cell cooling and gas humidification, thus making the electrochemical cells more cost-effective.

Evaporative cooling exploits the dissipation of the latent heat during the evaporation of the liquid, thus providing more efficient cooling than single-phase convection [5] and it enables removing the produced water in the form of vapor. In addition to electrochemical cells, evaporative cooling in porous media has many applications in energy engineering such as geothermal energy [6], soil science [7], building heat management [8], [9] or solar thermochemistry [10]. In PEM cells, the GDLs play an important role in the formation and transport of liquid water and gas. GDLs are porous structures connecting the catalyst layer, current collectors and gas flow channel. GDLs are specifically designed to facilitate the transport of molecules (be it reacting fuel or electrochemically-produced water), heat, and electrons. GDLs are thin porous media (typical

*Corresponding author: Tel.: +41 21 693 3878
Email address: sophia.haussener@epfl.ch (Sophia Haussener)

thickness $\leq 200\,\mu$m), with a porosity in the range of 65 to 90% [11], [12], [13], [14], pore sizes in the order of $10-40\,\mu$m, and typically made of carbon fibers with diameters in the range of $6-8\,\mu$m [15], [16]. The fibers in the GDLs offer solid struts for conductive heat transfer, a large surface area for convective heat transfer and an unsaturated pore space enhancing the evaporation rate [17], all benefiting the overall heat transfer [18], [19].

Water evaporation in GDLs has been investigated to understand the key driving mechanisms. General evaporation modeling approaches assume evaporation driven by the gradient of pressure or concentration of water vapor dissolved in the gas phase [20], [21], [22], [23]. He et al. [24] proposed a macroscopic model based on continuum mechanics for the specific case of evaporation in porous materials for PEM fuel cells (PEMFCs), utilizing effective properties to describe the heat and mass transport characteristics and a pressure gradient-driven evaporation rate. The kinetic theory of gases, which leads to the Hertz-Knudsen-Schrage (HKS) relation to evaluate the rate of phase-change at a liquid-vapor interface according to the local pressures and temperatures [25], has been used in general evaporation models [26], [27] and also in porous structures such as GDLs [28]. Safi et al. [15] utilized it within a numerical model for water evaporation in GDLs, with the vapor molar fraction at the evaporating interface acting as variable. However, their model was isothermal and the local temperature variations due to the cooling were not taken into account.

As implementing pore-scale models of real partially saturated GDLs based on experimental data is numerically and computationally challenging, Inoue et al. [29] designed an idealized geometrical model based on an artificial lattice to replace the actual porous media. The distance between each fiber, their diameter and the porosity were fixed to match actual GDL materials (specifically their pore size distribution). They showed that the evaporation rate depended on the GDL morphology, as the GDL morphology generated a specific topology of the liquid-gas interface area, where evaporation takes place.

A few studies focused on the optimization of the performance of the GDLs, i.e. to achieve efficient removal of heat and liquid water. The effects of operating conditions on phase-change were studied in a macroscopic model by Basu et al. [30]. They found that the relative humidity in the carrier gas flowing through the channel was key for the phase-change, as the amount of vapor in the channel and GDL limited the evaporation or condensation. Lal et al. [31] conducted experiments investigating the influence of temperature, carrier gas flow velocity, and carrier gas type on the evaporation rate. They reported that the velocity of the carrier gas had a small effect on evaporation, whereas increasing the temperature showed an exponential increase in the evaporation rate. They also pointed out that gas diffusivity alone, examined by modifying the carrier gas, could not explain the observed change in evaporation rate. Safi et al. [15], [32] utilized a combined experimental and numerical approach to test the influence of the carrier gas velocity in the channel on the evaporation rate. They showed that increasing the temperature promotes evaporation. Also, they observed that the evaporation rate of water in hydrogen carrier gas was higher than in air and was not limited by diffusion. However, the carrier gas speed they analyzed, ranging from $0.4\,$m/s to $1.6\,$m/s, were low compared to the $6\,$m/s velocity chosen by Lal et al. [31] for their reference case or compared to realistic operating conditions of PEM electrochemical cells.

As the majority of studies are based on in-situ, thereby stochastic, GDL structures, systematic investigations of the geometrical characteristics on the transport characteristics are not possible, hindering a more fundamental understanding and optimization of the evaporative cooling in porous structures. In this work, an actual GDL morphology was replicated by building a three-dimensional artificial lattice structure with the same porosity, average fiber size and pores size. The results of an analysis of the impact of several geometrical parameters on the evaporative cooling process within a porous media are presented, such as the porosity, the fiber size and the water saturation in the GDL, providing valuable guidelines to optimize the performance of GDLs in PEM-based electrochemical cells. In addition, many of the phase-change models considered isothermal approaches for modeling evaporative cooling in GDLs, overseeing the local temperature variations due to cooling in the GDL. In this study, evaporation at the liquid-vapor interface was modeled using kinetic theory, where the local pressures and temperatures at the interface were considered to calculate the interfacial mass transfer.

2. Numerical model

2.1. Fluid-solid model

A three-dimensional porous GDL sample was considered, inspired by a common GDL such as SGL 24BA as used, for example, by Safi et al. [15] (schematic in Fig. 1). The macroscopic properties of the structure (porosity, fiber diameter and pore size) were used as guidelines to construct a lattice structure approximating

real GDLs providing the opportunity for a more systematic investigation.

The GDL is composed of carbon fibers, whose bulk properties are defined as density ρ_{f}, specific heat $c_{p,\mathrm{f}}$ and thermal conductivity k_{f}. Liquid water is injected from the bottom of the GDL and therefore a water-gas interface forms within the GDL pores. At the water-gas interface evaporation takes place and, while water turns into steam, new water is introduced within the GDL to maintain a constant water level. The local evaporation rate, in terms of mass of vapor generated per unit time and interface area, is denoted as $\dot{m}''_{\mathrm{lv}}$. The top of the GDL is open to a channel where a controlled flow rate of gas is introduced. This carrier gas carries away the vapor generated within the GDL. At the channel outlet, a mixture of carrier gas and vapor exits the flow domain. This mixture is characterized by the mass fraction of the vapor (Y_{v}) and of the carrier gas ($1 - Y_{\mathrm{v}}$). In in-situ experiments, the water level in the GDL can be maintained constant and therefore at steady conditions the water-gas interface is static [15], [31]. The water region was modeled as a pseudo-solid that is separated from the gas region by a stationary and flat interface (Fig. 1). The density, specific heat and thermal conductivity of the water are ρ_{w}, $c_{p,\mathrm{w}}$ and k_{w}, respectively.

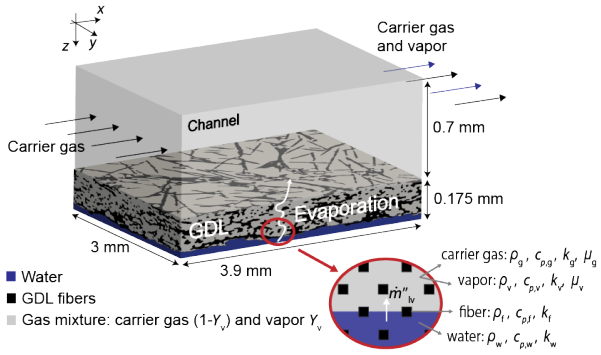

Figure 1: Illustration of the partially saturated GDL and channel on top. The carrier gas enters, sweeps the evaporated water away and exits as a mixture. The close-up look on the bottom-right shows the artificial GDL lattice considered in this work, partially saturated with water, with the properties to consider for each material.

2.2. Governing equations

The numerical model is based on the solution of the transient Navier-Stokes, species transport and energy conservation equations in the gaseous domain (carrier gas and steam mixture), and of the transient energy conservation equation in the solid domain (water and fibers). The properties of the carrier gas and water vapor mixture are defined as mass-averaged quantities. The mass conservation equation, solved in the fluid domain, is written as [33]:

$$\frac{\partial \rho}{\partial t} + \nabla \cdot (\rho \mathbf{u}) = \dot{m}''_{\mathrm{lv}} \delta \tag{1}$$

where $\mathbf{u}$ denotes the velocity, t the time, and $\dot{m}''_{\mathrm{lv}}$ the evaporation flux (in kg/(m^{2}s)). The vapor generation is treated as a mass source term. In order for the source term to be non-zero in computational cells adjacent to the water-gas interface only, the evaporation flux is multiplied by a $\delta-$function which represents the area of the interface divided by the volume of the cell (see Eq. (11)), and is different from zero only in cells next to the interface. This procedure is standard in interface-resolved simulations of flows with phase-change [18]. The remaining equations governing momentum conservation, species transport and energy conservation in the fluid domain are [33], [34]:

$$\frac{\partial (\rho \mathbf{u})}{\partial t} + \nabla \cdot (\rho \mathbf{u}\mathbf{u}) = -\nabla p + \nabla \cdot [\mu(\nabla \mathbf{u} + \nabla \mathbf{u}^T)] \tag{2}$$

where p is the pressure and μ the dynamic viscosity of the mixture,

$$\frac{\partial}{\partial t}(\rho Y_{\mathrm{v}}) + \nabla \cdot (\rho \mathbf{u} Y_{\mathrm{v}}) = -\nabla \cdot (-\rho D \nabla Y_{\mathrm{v}}) + \dot{m}''_{\mathrm{lv}} \delta \tag{3}$$

where D is the diffusion coefficient of the water vapor in the carrier gas, and:

$$\frac{\partial (\rho c_p T)}{\partial t} + \nabla \cdot (\rho c_p T \mathbf{u}) = \nabla \cdot (k \nabla T) + c_p (T - T_{\mathrm{ref}}) \dot{m}''_{\mathrm{lv}} \delta \tag{4}$$

where c_p is the constant pressure specific heat, T the temperature, and k the mass-averaged thermal conductivity of the mixture. The energy source term $c_p(T - T_{\mathrm{ref}})\dot{m}''_{\mathrm{lv}}\delta$ accounts for the enthalpy of the vapor generated by evaporation, where T_{ref} represents the reference temperature at which the vapor has zero enthalpy ($T_{\mathrm{ref}} = 298.15\,K$) [33].

For the water pseudo-solid domain, the energy conservation equation is solved with a negative source term that accounts for the removal of the latent heat resulting from water vaporization [33]:

$$\frac{\partial (\rho_{\mathrm{w}} c_{p,\mathrm{w}} T)}{\partial t} = \nabla \cdot (k_{\mathrm{w}} \nabla T) - h_{\mathrm{lv}} \dot{m}''_{\mathrm{lv}} \delta \tag{5}$$

with h_{lv} being the latent heat of vaporization. The same equation, without evaporation source term, is solved in the fiber solid domain:

$$\frac{\partial (\rho_{\mathrm{f}} c_{p,\mathrm{f}} T)}{\partial t} = \nabla \cdot (k_{\mathrm{f}} \nabla T) \tag{6}$$

where the bulk fiber properties are considered.

2.3. Evaporation model

In kinetic gas theory, the Maxwell-Boltzmann velocity distribution is adopted to express the speed of molecules in the gas and this can be utilised to estimate the flux of molecules through a flat surface per unit time and area [35]:

$$j = \left(\frac{m}{2\pi k_B T}\right)^{1/2} P_{sat}(T) \tag{7}$$

where k_B is the Boltzmann constant, P_{sat} is the equilibrium saturation pressure at the temperature T, and m is mass of one molecule. From the equation above, the net evaporation flux can be derived as the difference between the evaporation flux, i.e. the flux of molecules entering from the liquid into the vapor region, and the condensation flux, i.e. the flux of molecules transiting in the opposite direction. Knudsen revised this equation by introducing the phase-change coefficients, σ_e and σ_c for evaporation and condensation, respectively. Finally, the Hertz-Knudsen-Schrage equation was derived under the assumption that the values of the evaporation and condensation coefficients were equal [25]:

$$\dot{m}''_{lv} = \frac{2\sigma}{2-\sigma}\sqrt{\frac{m}{2\pi k_B}}\left(\frac{P_{sat}(T_I^l)}{\sqrt{T_I^l}} - \frac{P_I^v}{\sqrt{T_I^v}}\right) \tag{8}$$

where T_I^l and T_I^v are the temperatures on the liquid and vapor sides of the interface, respectively, $P_{sat}(T_I^l)$ is the equilibrium saturation pressure at T_I^l, and P_I^v is the partial pressure of vapor at the interface. $P_{sat}(T_I^l)$, T_I^l and T_I^v are calculated at the water-gas interface at each time-step, see the schematic in Fig. 2. P_I^v is the partial pressure of vapor and is therefore calculated as a function of the mole fraction of water vapor in the gas phase X_v at the water-gas interface [15]:

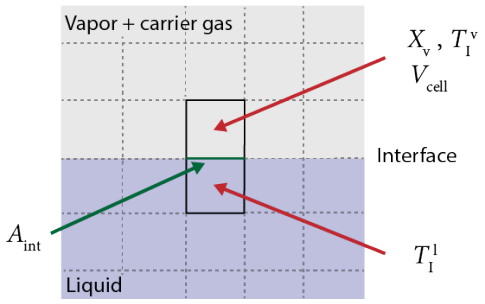

Figure 2: Illustration of the cells at the water-gas interface, where the liquid (water) and gas (vapor plus carrier gas) phases are in contact through the interfacial area A_{int}. The evaporation rate is evaluated in every gas cell next to the interface by knowledge of the local vapor mole fraction X_v, temperature T_I^v and volume of the cell V_{cell}, and of the liquid temperature T_I^l in the liquid adjacent cell.

$$P_I^v = X_v P_{amb} \tag{9}$$

where X_v is calculated based on the local vapor mass fraction:

$$X_v = \frac{Y_v/M_v}{Y_v/M_v + (1-Y_v)/M_g} \tag{10}$$

where M_v and M_g are the molecular weights of the vapor and carrier gas. In this study, the evaporation coefficient σ is taken as 0.37 following the work of Safi et al. [15], as they observed an optimal fit between their numerical model and experimental data with that evaporation coefficient. They considered thermophysical fluid properties and boundary conditions similar to the ones chosen in this study, thus motivating the choice of adopting their evaporation coefficient σ. P_{amb} is the atmospheric pressure. The interfacial area per cell volume [18] is estimated geometrically as (see Fig. 2):

$$\delta = \frac{A_{int}}{V_{cell}} \tag{11}$$

2.4. Discretization schemes

The governing equations introduced in Sec. 2.2 were solved in ANSYS Fluent and all the source terms related to evaporation (Sec. 2.3) were implemented using user-defined functions, similarly as described in [36], [18]. ANSYS Fluent adopts a finite-volume discretization of the flow equations, in a co-located grid arrangement. Pressure-velocity coupling is handled using the built-in ANSYS Fluent method [37], where the pressure is incorporated in the continuity equation by using the pressure-velocity relation obtained from the momentum equation. This pressure-based solver allows to solve the flow problem in either a segregated or coupled manner. The coupled approach was used, which solves the mass and momentum conservation equations implicitly, as it enables a pseudo transient formulation for time dependence, leading to a steady-state solution (regardless of the transient behaviour). The pseudo transient solution is an under-relaxation method, where the time dependence is controlled through a pseudo time step size, used to limit the evaporation source term per time step. The spatial derivatives in the energy, species, mass and momentum equations were discretized using a third-order monotone upstream-centered scheme for conservation law (MUSCL) [38]. The built-in PRESTO option (Pressure Staggering Option), which solves the pressure correction equation for a staggered control volume, was adopted. ANSYS Fluent uses iterative methods to

solve the systems of linear equations resulting from discretization and the convergence criteria were based on the residuals thresholds of 10^{-6} for mass and momentum conservation and species transport equations, and 10^{-12} for the energy conservation equation. The residuals thresholds were selected after an iteration convergence study. The pseudo time-step was set to 10^{-5} s. This value was chosen after a preliminary test of the results sensitivity to different time-step values.

2.5. Model geometry and boundary conditions

The simulation domain is a model of the experimental setup in Safi et al. [15], [32], where the authors extracted the GDL (SGL 24BA, with a porosity of 85% [12]) from a PEMFC and simplified the distribution of water by maintaining a constant water layer at the bottom of the GDL. The size of the GDL in the experiment (see Fig. 1) was (length×width×height) 3.9 mm×3 mm×0.175 mm. The top of the GDL was open to a channel of height 0.7 mm. The domain modeled in the simulations is shown in Fig. 3. To describe the geometry, a Cartesian reference frame is adopted where the coordinate x denotes the streamwise direction, y the transversal direction, and z the vertical direction, with the $z-$axis oriented downward. The origin of the axes is located at the top-left corner of the GDL. To reduce the computational cost, the transversal extension of the GDL was reduced from 3 mm to a value that described a unit cell's width, denoted as y_{GDL}, and depended on the fiber and pore size (defined below). Symmetry boundary conditions are used on the two lateral boundaries.

To replace the real GDL fiber structure, which is computationally challenging to reproduce in a full, representative pore-scale model, an artificial lattice structure was generated (see close-up view at bottom-left of Fig. 3). This enabled a more systematic investigation of the structural effects on the performance and operation. For meshing simplicity, the fibers are modeled as rods with square cross-section of size FS (fiber size). On a $x-z$ plane, the artificial GDL model consists of rows of fibers (colored in red and blue in Fig. 3), each fiber oriented along the y direction, where the rows are vertically staggered to increase the tortuosity of the GDL. The horizontal distance between the fibers of each row is denoted as PS (pore size). In order for the fibers to be in contact, and thus allow internal heat conduction, adjacent rows of fibers are in contact via longitudinally-oriented fibers (green in Fig. 3). From this lattice, the porosity ε of the GDL domain can be calculated. PS is calculated as a function of ε and FS. y_{GDL} is given by $\frac{1}{2}(PS + FS)$.
Water is considered to occupy the space among the fibers at the bottom of the GDL, with a horizontal flat water-gas interface. The amount of water in the GDL is quantified by the water saturation (WS), which is calculated as the percentage of the pore volume occupied by water. The geometrical and operational parameters FS, PS, ε and WS will be changed as part of our sensitivity

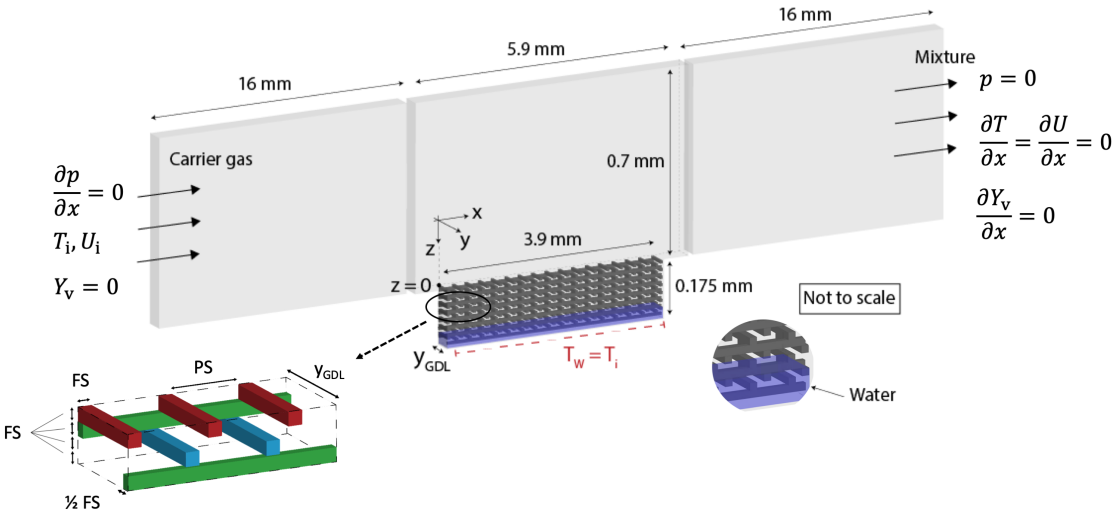

Figure 3: Schematic representation of the reference simulation domain, with partially saturated artificial lattice GDL (water saturation (WS) of 20%, represented in dark blue, shown in the close-up view on the bottom right). The close-up view on the bottom left illustrates the staggered disposition of the fibers in the artificial lattice. FS and PS stand for fiber and pore sizes, respectively. y_{GDL} denotes the width of the GDL considered in the simulations.

analysis in order to quantify their impact on the heat and mass transport processes within the GDL (see Sec. 4).

Temperature T (°C)	Diffusion coefficient D (cm^2/s)	
	air - vapor	hydrogen - vapor
30	0.2165	0.7874
60	0.2659	0.9452
80	0.2972	1.0560

Table 1: Temperature-dependent binary mass diffusion coefficients for air-vapor and hydrogen-vapor calculated with Chapman-Enskog theory [39].

The top of the GDL is connected to a channel of height 0.7 mm and total length of 37.9 mm, the latter arbitrarily chosen to avoid placing the inlet/outlet sections too close to the GDL. As boundary conditions at the inlet of the channel, the operating inlet velocity magnitude U_i and temperature T_i are imposed for the carrier gas with $Y_\mathrm{v} = 0$, and a zero-gradient condition for the pressure. At the outlet, zero-gradient conditions are set for velocity, temperature and vapor mass fraction, while the pressure is set to a constant reference value (1 atm). At the bottom boundary surface of the GDL, water is set at a constant temperature (T_w) to reproduce a uniform temperature as imposed to the system in the experiments [15], [32]. No-slip conditions are set on the fibers surfaces. All the other boundaries of the domain are treated as walls and as such no-slip and adiabatic conditions are set. The fluid properties for the carrier gas (either air or hydrogen) are considered at 1 atm [40]. The vapor properties are calculated for saturation conditions [41]. The diffusion constants for the binary mixture of vapor and carrier gas are calculated based on the Chapman-Enskog theory [39] and they are displayed in Tab. 1. The Chapman-Enskog theory is only valid for dilute cases while Stefan-Maxwell equations could give a more accurate approximation of the binary diffusion coefficient, as they do not require the designation of one species as a solvent. The Chapman-Enskog theory was chosen for simplicity.
The properties of bulk fiber and water are evaluated at a constant temperature of 60 °C, as preliminary tests suggested that their temperature had a negligible impact on the results, especially in the temperature range of relevance here. The bulk conductivity for carbon fiber in GDLs can vary in the range of $25 - 470\,\mathrm{W/(mK)}$ [42], [43], [44]. Average bulk thermal properties are considered, interpolated at 60 °C from available literature data [45], i.e. $k = 106.86\,\mathrm{W/(mK)}$, $\rho = 1760\,\mathrm{kg/m^3}$ and $c_p = 795.4\,\mathrm{J/(kgK)}$. The latent heat of vaporization for water is taken as $h_\mathrm{lv} = 2.26 \cdot 10^6\,\mathrm{J/kg}$ [46].
The computational domain is meshed with structured hexahedra cells. A mesh convergence study suggested mesh cell sizes of 2 μm in the GDL domain and in the section of the channel above it, and cell sizes of 5 μm in the inlet and outlet portions of the channel, were needed. The total number of cells ranges from 7 to 27 million, depending on y_GDL.

3. Validation

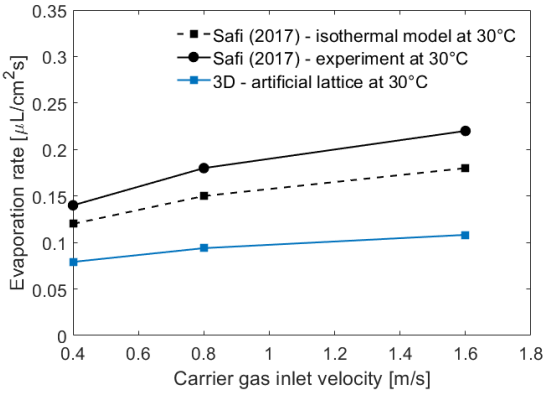

Figure 4: Comparison between computed and reported [15] evaporation rates as a function of carrier gas inlet velocities for SGL 24AB GDL and its artificial morphology equivalent (with macroscopic properties: $\varepsilon = 0.85$, $FS = 8\,\mu$m, $PS = 40.5\,\mu$m, $WS = 20\%$) for a fixed temperature $T_\mathrm{i} = T_\mathrm{w} = 30\,^\circ$C.

The results obtained with the present numerical model are compared to the experimental data and simulation results (with an isothermal model) of Safi et al. [15] for a SGL 24BA GDL. The real GDL is approximated by an artificial lattice represented with $\varepsilon = 0.85$, $FS = 8\,\mu$m, $PS = 40.5\,\mu$m, and $WS = 20\%$, values typical for SGL 24BA [12]. The models and experiments were conducted at $T_\mathrm{i} = 30\,^\circ$C and inlet air velocities ranged between 40 cm/s and 160 cm/s, values lower than typical PEMFC conditions [31]. The comparison is reported in Fig. 4, where the average evaporation rate obtained is shown for different velocities of the carrier gas, here air. The average evaporation rate is obtained by dividing the total evaporation rate by the projected GDL surface area, here calculated as the product of the streamwise GDL length (3.9 mm) and y_GDL. Our model captures well the monotonic increase of the evaporation rate with the velocity, and the decrease of the slope of the curve after 80 cm/s. The model underestimates by 47% the experimental data. This can be

GDL morphology	Porosity ε: 0.65, 0.7, 0.8, 0.9 Fiber size FS: 8, 16 μm Pore size PS: 12.9, 16.3, 28.5, 56.2, 65.4 μm
Operating conditions	Carrier gas inlet velocity U_i: 0.1, 0.5, 2, 6, 10, 12 m/s Temperature T_i and T_w: 30, 40, 50, 60, 70, 80 °C Water saturation WS: 20, 50, 80 %
Material properties	Carrier gas: air, H_2 Bulk fiber conductivity k_f: 10.6, 106, 1060 W/(mK)

Table 2: Summary of the operating conditions investigated in Sec. 4

attributed to the simplified liquid-gas interface configuration assumed in the present model, whereas the water profile in the GDL considered in Safi et al. [15] consists of the combination of different patterns, such as a layer of water and agglomeration of droplet patterns, which increases the interface surface area and therefore yields a higher evaporation rate. Different values of the evaporation coefficient σ were also tested, but these did not impact significantly the evaporation rate. Given the complexity of the multi-physics processes involved and the potential sources of deviation between experiments and simulations, our numerical model captures the experimental trends and magnitudes of the evaporation rate, and therefore it was concluded that the governing mechanisms are correctly represented.

4. Results

A parametric analysis was performed by varying three groups of parameters: the morphology of the GDL (ε and FS), the operating conditions (U_i, T_i, with $T_\mathrm{w} = T_\mathrm{i}$, and WS), and the material properties (carrier gas type and bulk fiber conductivity k_f). A list of the parameters varied and their values is provided in Tab. 2. The analysis focused on the evaporation rate, as the removal of the latent heat resulting from water evaporation (and leading to the cooling of the GDL) is proportional to the evaporation rate.

4.1. Reference case

The reference case is run with an artificial GDL of $\varepsilon = 0.8$, $FS = 8\,\mu$m and $PS = 28.5\,\mu$m, air as carrier gas entering the channel at $U_\mathrm{i} = 6\,$m/s and $T_\mathrm{w} = 60\,^\circ$C (with $T_\mathrm{w} = T_\mathrm{i} = 60\,^\circ$C), and $WS = 20\%$. The GDL thickness y_GDL is 18.3 μm and the bulk thermal conductivity of the fiber is $k_\mathrm{f} = 106\,$W/(mK).

The velocity contours within the gas channel and the GDL region are depicted in Fig. 5, where they are extracted on a $x-z$ cross-section located at $y_\mathrm{GDL}/2$. The flow is laminar under the entire set of carrier gas velocities tested in this work [47] (i.e. $\mathrm{Re} = UD/\nu = 400$, where U is the mean velocity of the carrier gas, D the

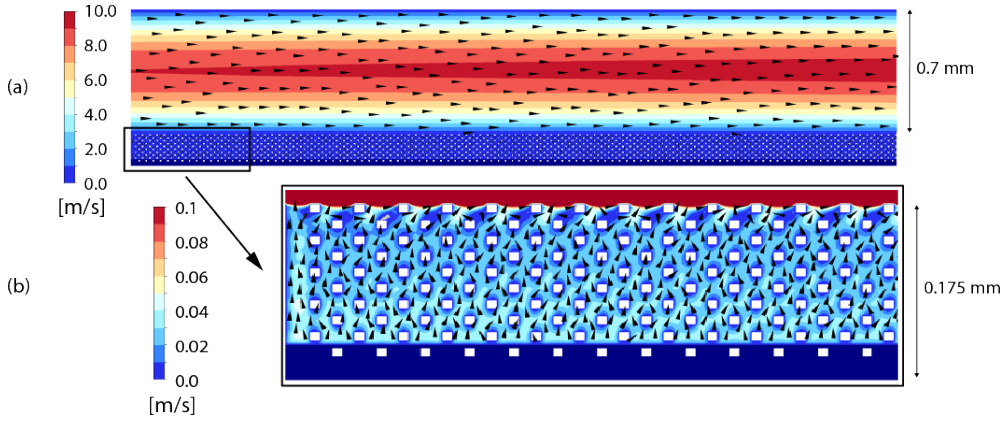

Figure 5: Velocity contours and vectors in the (a) gas channel and (b) GDL, extracted on a $x-z$ slice located at $y_\mathrm{GDL}/2$, for the reference case. In (b), the velocity is rescaled to better illustrate the velocity field in the GDL. The region occupied by the water can be identified as the region where the velocity is zero (colored in dark blue).

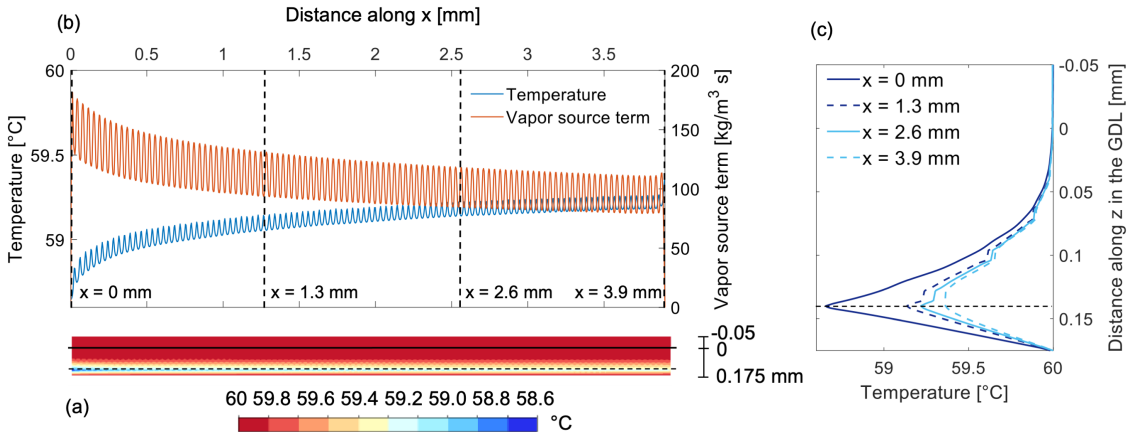

Figure 6: (a) Temperature contours in the GDL extracted on a $x-z$ slice located at $y_{\mathrm{GDL}}/2$. The dashed horizontal line locates the water-gas interface, which is also indicated in (c) with a dashed line. The solid horizontal line indicates the transition between the GDL and the channel. (b) Temperature and vapor source term at the water-gas interface ($z = 0.14$ mm) versus the streamwise direction x. (c) Temperature profiles in the GDL extracted over the black dashed vertical lines indicated in (b). The vapor source term in (b) and the temperature profiles in (b) and (c) are averaged along the width (y) direction. The results are shown for the reference case.

diameter of the channel and ν the kinematic viscosity of the carrier gas), and a parabolic velocity profile develops within the gas channel as the flow proceeds downstream. Water evaporates at the water-gas interface in the GDL and vapor penetrates through the porous region until it reaches the top of the GDL and is then swept away by the gas. The vapor velocity in the GDL is of about 0.05 m/s, thus two orders of magnitude smaller than the gas velocity in the channel. The evaporation of water is limited by the humidity (amount of vapor in the carrier gas) of the gas above the water-gas interface, as this impacts the vapor pressure which enters Eq. (8), and therefore the transport mode of vapor removal from the GDL is of interest. The Péclet number of the vapor flow in the GDL (i.e. $\mathrm{Pe} = UL/D \ll 1$, with U being the vapor velocity, L the pore size and D the diffusion coefficient of water vapor in air) suggests that diffusion dominates over convection.

A thermal analysis of the GDL is presented in Fig. 6, where the temperature contours on a $x-z$ slice located at $y_{GDL}/2$ are reported at the water-gas interface, along with the temperature of the water-gas interface and the vapor source term (averaged along the width (y) direction). The vertical profiles of temperature within the GDL at selected streamwise locations are also represented in Fig. 6. The temperature field reveals the cooling effect of the evaporation at the water-gas interface, with the temperature decreasing by about 1.4 °C from the boundary value of 60 °C. The oscillations in both the temperature and vapor source term are due to the presence of the fibers in the y direction. The vapor source term decreases along x as the vapor molar fraction of the gas increases due to generation of vapor. This reduces the rate of latent heat removed by the evaporation process and, therefore, the temperature of the interface increases along x, emphasizing a reduction of the cooling effect (see also the vertical temperature profiles in Fig. 6(c)).

This reference case suggests that the GDL morphology, operational flow rates and temperatures, and fluid/solid properties may all influence the evaporation dynamics and cooling effect.

4.2. *Effect of the morphology*

The porosity is varied from 0.65 to 0.9, while maintaining the fiber size at 8 μm and the water saturation at 20%. For each value of the porosity analyzed, the carrier gas velocity is changed between $U_{\mathrm{i}} = 0.1$ m/s and 12 m/s. All the other conditions are kept at reference conditions. The evaporation rates obtained in these conditions are displayed in Fig. 7. The evaporation rate decreases by 22.3% when decreasing porosity from 0.8 to 0.65, and increases by 19.9% when increasing porosity from 0.8 to 0.9. As the evaporation rate is calculated by taking the total evaporation rate divided by the projected GDL area, the increase of evaporation rate with porosity is directly linked to the increasing water-gas interface area when porosity increases. The inset in Fig. 7 shows the evaporation rate at a fixed U_{i}, rescaled with both, the projected GDL area and the actual water-gas interface area, for $\varepsilon = 0.65 - 0.9$.

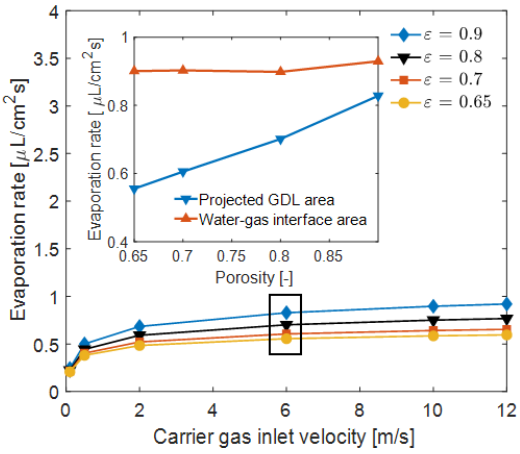

Figure 7: Analysis of the effect of GDL porosity on the average evaporation rate, normalized by the projected GDL surface area. The inset compares the evaporation rates at $U_i = 6\,\mathrm{m/s}$, normalized with the projected GDL surface area and with the actual water-gas interfacial area. Simulation conditions are from the reference case except for: $\varepsilon = 0.65 - 0.9$ and $U_i = 0.1 - 12\,\mathrm{m/s}$.

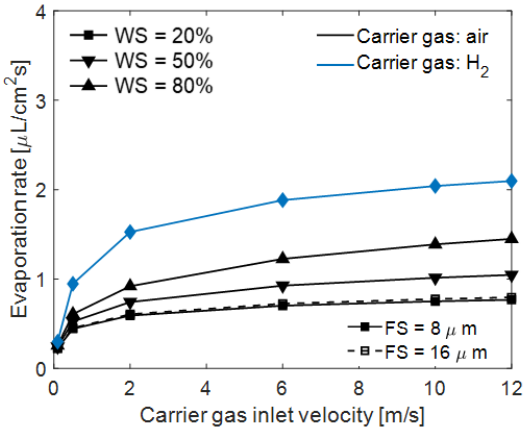

Figure 8: Influence of FS, WS and the carrier gas type on the evaporation rate for $U_i = 0.1 - 12\,\mathrm{m/s}$. The simulation conditions are varied from the reference case. The increase of FS, and consequently PS, shows a minor influence on the evaporation rate, while the rising water saturation WS and the type of carrier gas significantly affect the evaporation rate.

Indeed, the evaporation rate rescaled with the actual interface area is constant for $\varepsilon = 0.65-0.8$ and increases only at $\varepsilon = 0.9$. It is hypothesized that this increase is related to the increase in the permeability of the artificial porous structure. As the permeability increases non-linearly with the porosity [48], this effect becomes more prominent for very large porosities. A larger permeability allows for the vapor to escape the GDL more easily, thus leading to a lower vapor molar fraction near the interface and, therefore, resulting in a higher evaporation rate.

Increasing the fiber size from $8\,\mu$m to $16\,\mu$m at constant porosity of 0.8 while increasing the carrier gas inlet velocity did show a minor effect on the evaporation rate (see Fig. 8). An increase in fiber size by a factor of two instigated a 3.5% increase in the evaporation rate only. Keeping a constant reference porosity but increasing the fiber size leads to a larger distance between the fibers PS (from $28.5\,\mu$m to $56.2\,\mu$m). Since the water-gas interface area is the same, this effect is related to the enhanced permeability resulting from a larger distance between the fibers (i.e. larger pore size), which reduces the vapor molar fraction of the gas above the interface.

4.3. Effect of the operating conditions

The impact of the water saturation was tested by varying the saturation from 20% to 80% while maintaining all other conditions at reference level. Figure 8 displays the evaporation rate obtained as a function of the carrier gas velocity and WS. The evaporation rate increases with WS. Increasing the water saturation by a factor 4 yields an increase of the evaporation rate by a factor 1.88 (or 88%). Indeed, as the water-gas interface moves closer to the channel, the distance for the vapor to travel in order to leave the GDL domain is greatly reduced. Thus the outflow of vapor is facilitated and the humidity of the gas in the GDL reduced, increasing the driving force for evaporation.

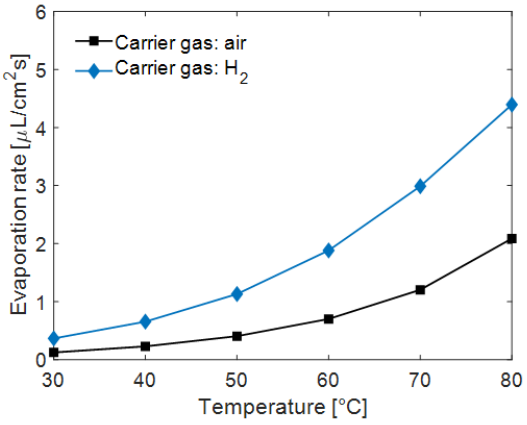

Figure 9: Influence of T_i and the carrier gas type (air or hydrogen) on the evaporation rate, with other conditions at reference. For the tested range of temperatures ($T_i = 30-80\,^\circ\mathrm{C}$), the evaporation rate increases exponentially. H_2 as carrier gas increased the evaporation compared to air.

When inspecting the influence of the carrier gas velocity (Fig. 8), the evaporation rate was observed to increase monotonically with U_i and this increase saturated at larger velocities. The diffusion of vapor across the GDL and its removal by convection by the carrier gas at the top of the GDL can be thought as two processes that occur in series, each with its own resistance. When the carrier gas speed is increased from very low values, the resistance associated to the convective process drops, thus yielding a significant increase of the evaporation rate. However, at larger values of U_i, the convective resistance becomes negligible compared to that associated to the mass diffusion in the GDL, which is independent of U_i, and therefore the evaporation rate reaches an asymptotic limit. By heat transfer analogy, the resistance to mass diffusion in the GDL is inversely proportional to the water level (i.e. the distance between the water-gas interface and the top of the GDL), and therefore the saturation of the evaporation rate occurs at higher U_i for larger WS.
In order to investigate the impact of the operational temperature, the gas inlet and water temperatures were varied between $T_i = T_w = 30\,^\circ\mathrm{C}$ and $T_i = T_w = 80\,^\circ\mathrm{C}$, while keeping all the other parameters at reference conditions.

Figure 9 indicates that the evaporation rate follows an exponential trend with the temperature, and when increasing the temperature from 60 °C to 80 °C, the evaporation rate increases with a factor 2.97 (or by 197%). Although the increase of the temperatures T_I^l and T_I^v should lead to a decrease of the evaporation rate $\dot{m}''_{lv}$ as they are in the denominator of Eq. (8), the saturation pressure $P_{sat}(T_I^l)$ increases by a factor 11 when increasing the temperatures from 303 K to 353 K, thus driving the increase of the evaporation rate.

4.4. Effect of the material properties

Figures 8 and 9 show the effect of the change of the carrier gas (i.e. its thermophysical properties) on the evaporation rate. Specifically, air was exchanged by hydrogen.

Generally, hydrogen leads to significantly higher evaporation rates than air, and this increase is more pronounced at lower velocities U_i, where mass diffusion dominates, and with increasing T_i. At 60 °C and 6 m/s, the evaporation rate increases by a factor 2.7 when exchanging air by hydrogen as carrier gas. The better performance of hydrogen can be directly linked to the larger diffusion coefficient of vapor in hydrogen, with $D = 0.9452\,\mathrm{cm^2/s}$ at 60 °C, as opposed to $D = 0.2659\,\mathrm{cm^2/s}$ at 60 °C of vapor in air. This facilitates the diffusion of vapor away from the interface, enabling the reduction of the humidity in the interface cells, thus leading to a higher evaporation rate. Furthermore, the molecular weight of hydrogen is much smaller than that of air. This impacts the humidity of the gas, see Eq. (10), where a lower M_g leads to a lower X_v for same M_v and Y_v, i.e. hydrogen can absorb more vapor due to its lower molecular density, thus promoting water evaporation. The larger evaporation rate induced by hydrogen is reflected on the distribution of the vapor

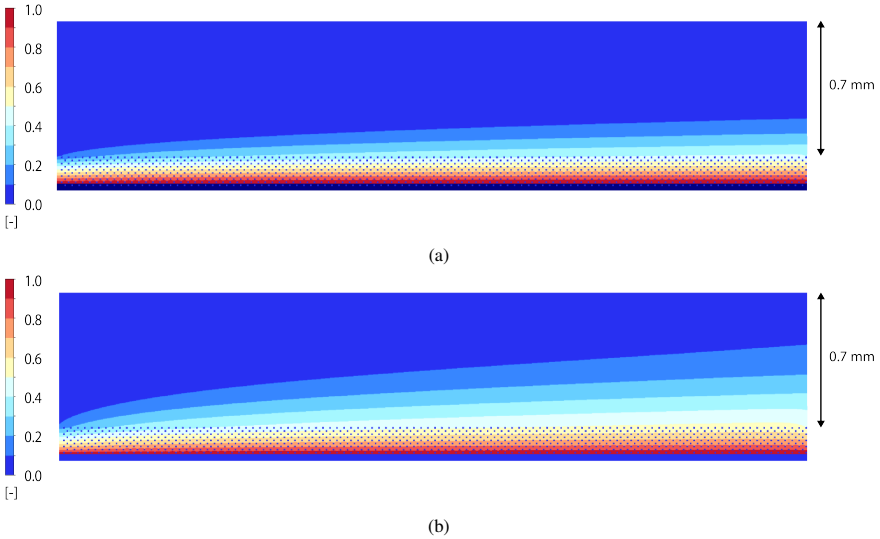

Figure 10: Contour of the relative humidity of the carrier gas. The relative humidity is extracted on a slice located at $y_{GDL}/2$ for (a) air and (b) hydrogen as carrier gas. The simulation conditions are at reference conditions.

within the gas channel. Figure 10 depicts the contours of the relative humidity of the carrier gas in the flow domain and it can be seen that a wet boundary layer develops in the channel above the GDL, as effect of the introduction of vapor, and this boundary layer is 2 times thicker in the presence of hydrogen.

The conductivity of the bulk fibers was varied by two orders of magnitude (from 10.6 W/(mK) to 1060 W/(mK)). The carrier gas velocity was maintained at $U_i = 6\,\mathrm{m/s}$, with T_i and T_w varied between 30 °C and 80 °C. The results of this analysis indicated that the fiber conductivity has a negligible influence on the evaporation rate, i.e. the evaporation rates varied by less than 0.2%. As the heat conductivity of the fibers is orders of magnitude larger than that of the water-gas mixture, the diffusion of heat in the GDL is always limited by diffusion in the fluid region. The heat flux was observed to be directed towards the water-gas interface, both from the bottom surface of the GDL and the top surface of the GDL (i.e. the surface in contact with the channel). The heat is transported to the water-gas interface, where it is absorbed by the heat sink due to evaporation. Thus, the heat flux is defined by the magnitude of the evaporation sink term. The temperature at the water-gas interface decreases (see Fig. 6) as a result of this heat flux. For the reference case, the heat is mostly conducted through the fibers (i.e. 79% of the total flux at the channel-GDL interface is transported through the fibers), given their relatively large thermal conductivity and the temperature gradient in the various phases of the GDL is similar. Indeed, if the temperature gradient is the same for all three phases (fibers, water, gas), the heat flux only depends on the value of the thermal conductivity.

5. Conclusions and future work

A coupled heat and mass transfer numerical model with evaporation is developed to analyze the main parameters influencing the evaporative cooling capability in a GDL. The GDL's geometry is approximated by an artificial lattice, which allows to systematically investigate the effect of geometrical characteristics on the GDL's transport and evaporation.

Overall, the effect of the GDL geometry on the evaporative cooling was small. Increasing the porosity from 0.8 to 0.9 enhanced the evaporation by 19.9%, which could be explained by the increase of the water-gas interface area and the non-linear augmentation of permeability with porosity. Applying a factor 2 to the fiber size while maintaining a constant porosity led to a 3.5% enhancement of evaporation rate, due to the larger distance between fibers and thus higher permeability.

The operating conditions induced a much larger impact on the evaporation rate, which showed to be mostly limited by the diffusion of the water vapor in the carrier gas. Increasing the water saturation from 20% to 80% led to a 88% enhancement in evaporation, due to the reduction of the distance between water-gas interface and channel, therefore facilitating the transport of vapor into the channel and its removal by advection. Evaporation was enhanced by 197% when increasing the GDL bottom temperature from 60 °C to 80 °C, as a higher temperature allows for a larger mass fraction of vapor in the gas mixture. Changing the carrier gas properties resulted in the largest impact on evaporation, i.e. an increase by a factor 2.7 when changing from air to H_2. The binary coefficient for diffusion of the gas mixture is a key parameter for increasing the evaporation rate. Helium would also be an interesting carrier gas choice, as the binary diffusion coefficient is even higher than what was tested in the present model (i.e. $D_{He/H_2O} = 1.028\,\mathrm{cm^2/s}$ at 60 °C).

The developed pore-level model allows for the quantification of the variability in temperature, velocity, species concentration, and evaporation rate within the porous media and highlights that these variations are significant. Consequently, reported macroscopic evaporation rates need to be carefully interpreted. Furthermore, electrochemical devices (such as fuel cells or electrolyzers) typically have channel-rib structures in their flow field, introducing additional heterogeneity that might be superimposed on top of the pore-level variations, further exacerbating local variations in the evaporation rate. In order to investigate this, the developed pore-level evaporation model can be incorporated in a full device model (for example PEMFC model) in order to analyze the effect of the local conditions under the rib or in the channel, and their effect on the evaporation rate. In turn, such an analysis can be used to design the optimal GDL structure (potentially varying under the rib and in the channel) that allows for a better removal of the vapor in order to maximize the evaporative cooling. Furthermore, our numerical simulations assumed a flat water interface thus neglecting a more realistic distribution of the water. In the future, the numerical model could be applied to realistic geometries of partially saturated GDLs obtained from in-situ and in-operando tomography scans and provide specific guidelines for a particular GDL and saturation state. With the model at hand, we deconvoluted the effect of geometry, operating condition, and material characteristics on the evaporation in porous structures and provided a first, simplified de-

sign tool for GDL's and, more broadly, porous structures used in evaporative cooling applications.

6. Acknowledgments

The authors would like to thank the Swiss National Science Foundation for their financial support under the grant #200021_169913 and the associated mobility grant. We thank Felix N. Büchi, Jens Eller and Adrian Mularczyk from PSI (Paul Scherrer Institute) Villigen, Switzerland, for useful discussion and experimental data.

Nomenclature

English symbols

$\dot{m}''$	mass flux	$kg/(m^2s)$
$\mathbf{u}$	velocity	m/s
A	area	m^2
c_p	specific heat	$J/(kgK)$
D	mass diffusion coefficient	m^2/s
FS	fiber size	m
h	latent heat	J/kg
j	flux	$kg/(m^2s)$
k	heat conductivity	$W/(mK)$
k_B	Boltzmann constant	$(m^2kg)/(sK)$
L	characteristic length	m
M	molecular weight	g/mol
m	mass	kg
$P,\ p$	pressure	Pa
PS	pore size	m
T	temperature	K, °C
t	time	s
V	volume	m^3
WS	water saturation	–
X	mole fraction	–
Y	mass fraction	–

Greek Symbols

δ	interfacial area per volume	m^2/m^3
μ	dynamic viscosity	Pas
ρ	density	kg/m^3
ε	porosity	–

Subscripts

amb	ambient
c	condensation
e	evaporation
f	fiber
g	carrier gas
I	interface
i	inlet
lv	liquid-vapor
l	liquid
max	maximum
min	minimum
ref	reference
sat	saturation
v	water vapor
w	water

7. References

References

References

[1] I. Staffell, D. Scamman, A. Velazquez Abad, P. Balcombe, P. E. Dodds, P. Ekins, N. Shah, and K. R. Ward. The role of hydrogen and fuel cells in the global energy system. *Energy and Environmental Science*, 12(2):463–491, 2019.

[2] Marcelo Carmo, David L. Fritz, Jürgen Mergel, and Detlef Stolten. A comprehensive review on PEM water electrolysis. *International Journal of Hydrogen Energy*, 38(12): 4901–4934, 2013.

[3] I. Bar-On, R. Kirchain, and R. Roth. Technical cost analysis for PEM fuel cells. *Journal of Power Sources*, 109(1): 71–75, 2002.

[4] P. Mock and S. A. Schmid. Fuel cells for automotive powertrains-A techno-economic assessment. *Journal of Power Sources*, 190(1):133–140, 2009.

[5] S. H. Hwang and M.S. Kim. An experimental study on the cathode humidification and evaporative cooling of polymer electrolyte membrane fuel cells using direct water injection method at high current densities. *Applied Thermal Engineering*, 99:635–644, 2016.

[6] P. Cheng. Heat Transfer in Geothermal Systems. *Advances in Heat Transfer*, 14:1–105, 1979.

[7] W. K. Song and Y. J. Cui. Modelling of water evaporation from cracked clayey soil. *Engineering Geology*, 266 (December 2019):105465, 2020.

[8] A. K. Nayak, A. Hagishima, and J. Tanimoto. A simplified numerical model for evaporative cooling by water spray over roof surfaces. *Applied Thermal Engineering*, 165(October 2019):114514, 2020.

[9] G. Leroux, N. Le Pierrès, L. Stephan, E. Wurtz, J. Anger, and L. Mora. Pilot-scale experimental study of an innovative low-energy and low-cost cooling system for buildings. *Applied Thermal Engineering*, 157(April):113665, 2019.

[10] T. Liu, Z. Bai, Z.i Zheng, Q. Liu, J. Lei, J. Sui, and H. Jin. 100 kWe power generation pilot plant with a solar thermochemical process: design, modeling, construction, and testing. *Applied Energy*, 251(April):113217, 2019.

[11] I. V. Zenyuk, A. Lamibrac, J. Eller, D. Y. Parkinson, F. Marone, F. N. Büchi, and A. Z. Weber. Investigating Evaporation in Gas Diffusion Layers for Fuel Cells with X-ray Computed Tomography. *The Journal of Physical Chemistry C*, 120(50):28701–28711, 2016.

[12] R. R. Rashapov, J. Unno, and J. T. Gostick. Characterization of PEMFC Gas Diffusion Layer Porosity. *Journal of The Electrochemical Society*, 162(6):F603–F612, 2015.

[13] A. El-Kharouf, T. J. Mason, D. J. L. Brett, and B. G. Pollet. Ex-situ characterisation of gas diffusion layers for proton exchange membrane fuel cells. *Journal of Power Sources*, 218:393–404, 2012.

[14] R. Flückiger, S. A. Freunberger, D. Kramer, A. Wokaun, G. G. Scherer, and F. N. Büchi. Anisotropic, effective diffusivity of porous gas diffusion layer materials for PEFC. *Electrochimica Acta*, 54(2):551–559, 2008.

[15] M. A. Safi, N. I. Prasianakis, J. Mantzaras, A. Lamibrac, and F. N. Büchi. Experimental and pore-level numerical investigation of water evaporation in gas diffusion layers of polymer electrolyte fuel cells. *International Journal of Heat and Mass Transfer*, 115:238–249, 2017.

[16] S. M. Moosavi, M. Niffeler, J. T. Gostick, and S. Haussener. Transport characteristics of saturated gas diffusion layers treated with hydrophobic coatings. *Chemical Engineering Science*, 176:503–514, 2017.

[17] D. P. Mondal, S. Das, A. Badkul, and N. Jha. Modelling of evaporative cooling of porous medium filled with evaporative liquid. *Computers, Materials and Continua*, 13(2): 115–134, 2010.

[18] M. Magnini, B. Pulvirenti, and J. R. Thome. Numerical investigation of hydrodynamics and heat transfer of elongated bubbles during flow boiling in a microchannel. *International Journal of Heat and Mass Transfer*, 59(1): 451–471, 2013.

[19] P. Smakulski and S. Pietrowicz. A review of the capabilities of high heat flux removal by porous materials, microchannels and spray cooling techniques. *Applied Thermal Engineering*, 104:636–646, 2016.

[20] W. M. Kays and M. E. Crawford. *Convective Heat and Mass Transfer*. McGraw-Hill Science/Engineering/Math, 3 edition edition, 1993.

[21] A. A. Shah, G. S. Kim, W. Gervais, A. Young, K. Promislow, J. Li, and S. Ye. The effects of water and microstructure on the performance of polymer electrolyte fuel cells. *Journal of Power Sources*, 160(2 SPEC. ISS.):1251–1268, 2006.

[22] O. Chapuis, M. Prat, M. Quintard, E. Chane-Kane, O. Guillot, and N. Mayer. Two-phase flow and evaporation in model fibrous media. Application to the gas diffusion layer of PEM fuel cells. *Journal of Power Sources*, 178(1):258–268, 2008.

[23] T. A. H. Nguyen, A. V. Nguyen, M. A. Hampton, Z. P. Xu, L. Huang, and V. Rudolph. Theoretical and experimental analysis of droplet evaporation on solid surfaces. *Chemical Engineering Science*, 69(1):522–529, 2012.

[24] W. He, J. S. Yi, and T. Van Nguyen. Two-phase flow model of the cathode of PEM fuel cells using interdigitated flow fields. *AIChE Journal*, 46(10):2053–2064, 2000.

[25] R. W. Schrage. *A Theoretical Study of Interphase Mass Transfer*. Columbia University Press, New York, 1953.

[26] M. Bond and H. Struchtrup. Mean evaporation and condensation coefficients based on energy dependent condensation probability. *Physical Review E - Statistical Physics, Plasmas, Fluids, and Related Interdisciplinary Topics*, 70 (6):21, 2004.

[27] Q. Li, K. Zhao, and Y. M. Xuan. Simulation of flow and heat transfer with evaporation in a porous wick of a CPL evaporator on pore scale by lattice Boltzmann method. *International Journal of Heat and Mass Transfer*, 54(13-14): 2890–2901, 2011.

[28] A. H. Persad and Charles A. Ward. Expressions for the Evaporation and Condensation Coefficients in the Hertz-Knudsen Relation. *Chemical Reviews*, 116(14):7727–7767, 2016.

[29] G. Inoue, N. Ishibe, Y. Matsukuma, and M. Minemoto. Simulation of Liquid Water Evaporation in GDL for PEMFC Under Gas Purge Condition. *ASME-JSME-KSME 2011 Joint Fluids Engineering Conference*, pages 3585–3591, 2011.

[30] S. Basu, C. Y. Wang, and K. S. Chen. Phase Change in a Polymer Electrolyte Fuel Cell. *Journal of the Electrochemical Society*, 156:B748–B756, 2009.

[31] S. Lal, A. Lamibrac, J. Eller, and F. N. Büchi. Determination of Water Evaporation Rates in Gas Diffusion Layers of Fuel Cells. *Journal of The Electrochemical Society*, 165 (9):F652–F661, 2018.

[32] M. A. Safi, J. Mantzaras, N. I. Prasianakis, A. Lamibrac, and F. N. Büchi. A pore-level direct numerical investigation of water evaporation characteristics under air and hydrogen in the gas diffusion layers of polymer electrolyte fuel cells. *International Journal of Heat and Mass Transfer*, 129:1250–1262, 2019.

[33] S. Hardt and F. Wondra. Evaporation model for interfacial flows based on a continuum-field representation of the source terms. *Journal of Computational Physics*, 227(11): 5871–5895, 2008.

[34] A. Z. Weber, R. L. Borup, R. M. Darling, P. K. Das, T. J. Dursch, W. Gu, D. Harvey, A. Kusoglu, S. Litster, M. M. Mench, R. Mukundan, J. P. Owejan, J. G. Pharoah, M. Secanell, and I. V. Zenyuk. A Critical Review of Modeling Transport Phenomena in Polymer-Electrolyte Fuel Cells. *Journal of the Electrochemical Society*, 161(12):F1254–F1299, 2014.

[35] V. P Carey. *Liquid Vapor Phase Change Phenomena: An Introduction to the Thermophysics of Vaporization and Condensation Processes in Heat Transfer Equipment, Second Edition*. Taylor & Francis, 1992.

[36] M. Fiorentino and G. Starace. Numerical investigations on

two-phase flow modes in evaporative condensers. *Applied Thermal Engineering*, 94:777–785, 2016.

[37] Ansys Inc. ANSYS Fluent User's Guide 19.2, 2018.

[38] B. Van Leer. Towards the ultimate conservative difference scheme. IV. A new approach to numerical convection. *Journal of Computational Physics*, 23(3):276–299, 1977.

[39] E. L. Cussler. *Diffusion, Mass Transfer in Fluid Systems*. Cambridge University Press, 3rd edition edition, 2009.

[40] Y. A. Cengel and J. M. Cimbala. *Fluid Mechanics Fundamentals and Applications*. McGraw-Hill, 3rd edition, 2014.

[41] E. W. Lemmon, M. O. McLinden, and D. G. Friend. Thermophysical Properties of Fluid Systems. In P.J. Linstrom and W.G. Mallard, editors, *WebBook de Chimie NIST, Standard Reference Database NIST Number 69*. National Institue of Standards and Technology, 2019.

[42] I. Nitta, O. Himanen, and M. Mikkola. Thermal conductivity and contact resistance of compressed gas diffusion layer of PEM fuel cell. *Fuel Cells*, 8(2):111–119, 2008.

[43] J. Ramousse, S. Didierjean, O. Lottin, and D. Maillet. Estimation of the effective thermal conductivity of carbon felts used as PEMFC Gas Diffusion Layers. *International Journal of Thermal Sciences*, 47(1):1–6, 2008.

[44] E. Sadeghi, M. Bahrami, and N. Djilali. Analytic determination of the effective thermal conductivity of PEM fuel cell gas diffusion layers. *Journal of Power Sources*, 179 (1):200–208, 2008.

[45] N. Zamel, X. Li, and J. Shen. Correlation for the effective gas diffusion coefficient in carbon paper diffusion media. *Energy and Fuels*, 23(12):6070–6078, 2009.

[46] V. Singh, P. Singh, and U. K. Haritashya. *Encyclopedia of Snow, Ice and Glaciers*. Springer, 2011.

[47] H. Liu, G. Zhang, D. Li, C. Wang, S. Bai, G. Li, and G. Wang. Three-dimensional multi-phase simulation of cooling patterns for proton exchange membrane fuel cell based on a modified Bruggeman equation. *Applied Thermal Engineering*, 174(April), 2020.

[48] S. Suter, A. Steinfeld, and S. Haussener. Pore-level engineering of macroporous media for increased performance of solar-driven thermochemical fuel processing. *International Journal of Heat and Mass Transfer*, 78:688–698, 2014.